

# Equilibrium concentration profiles and sedimentation kinetics of colloidal gels under gravitational stress

S. Buzzaccaro<sup>1</sup>, E. Secchi<sup>1</sup>, G. Brambilla<sup>2,3,4</sup>, R. Piazza<sup>1</sup>, L. Cipelletti<sup>2,3</sup>

<sup>1</sup>Dipartimento di Chimica, Politecnico di Milano, 20131 Milano, Italy

<sup>2</sup>Université Montpellier 2, Laboratoire Charles Coulomb UMR 5221, F-34095, Montpellier, France

<sup>3</sup>CNRS, Laboratoire Charles Coulomb UMR 5221, F-34095, Montpellier, France <sup>4</sup>

Present address: Formulacion, L'Union, France.

E-mail: stefano.buzzaccaro@mail.polimi.it, luca.cipelletti@univ-montp2.fr

**Abstract.** We study the sedimentation of colloidal gels by using a combination of light scattering, polarimetry and video imaging. The asymptotic concentration profiles  $\varphi(z, t \rightarrow \infty)$  exhibit remarkable scaling properties: profiles for gels prepared at different initial volume fractions and particle interactions can be superimposed onto a single master curve by using suitable reduced variables. We show theoretically that this behavior stems from a power law dependence of the compressive elastic modulus *vs*  $\varphi$ , which we directly test experimentally. The sedimentation kinetics comprises an initial latency stage, followed by a rapid collapse where the gel height  $h$  decreases at constant velocity, and a final compaction stage characterized by a stretched exponential relaxation of  $h$  towards a plateau. Analogies and differences with previous works are briefly discussed.

PACS numbers: 47.57.ef, 64.70.pv, 82.70.Dd

Submitted to: *J. Phys.: Condens. Matter*

## 1. Introduction

Colloidal gels are the focus of an intensive research effort for both fundamental and practical reasons. On the one hand, they are model systems to understand the interplay between percolation, phase separation and dynamical arrest in systems with attractive interactions [1, 2, 3]. On the other hand, colloidal gels are ubiquitous, e.g., in the food, drug, personal care and cosmetic industries, where they are often used as a means to stabilize a complex formulation against macroscopic phase separation. Mechanically, colloidal gels are viscoelastic systems with a predominantly solid-like behavior. However, they typically yield under a modest stress, often including the gravitational stress

exerted by their own weight. It is therefore not surprising that many studies have been devoted to the sedimentation behavior of colloidal gels, revealing a wealth of fascinating but yet not fully understood phenomena, such as delayed sedimentation [4, 5, 6, 7, 8], creep [4, 9, 10, 11, 12], and fracture associated with complex flow patterns [4, 9, 13]. With a few notable exceptions [4, 6, 8], most previous work has focussed on the macroscopic behavior of the gels, typically by measuring the time evolution of the gel height,  $h(t)$ . This has prevented a thorough test of the various models proposed to rationalize the gel behavior, and in particular of the poroelastic model [14, 15].

To overcome these limitations, we have recently reported in Ref. [16] a full characterization of the temporal evolution of the concentration profile,  $\varphi(z, t)$ , sedimentation velocity profile,  $v(z, t)$  and microscopic rearrangement dynamics of a colloidal gel. In particular, we have shown that the poroelastic model captures remarkably well the evolution of  $h(t)$ ,  $\varphi(z, t)$  and  $v(z, t)$ . Additionally, a single quantity, the compressive strain rate  $\dot{\epsilon}(t)$ , was shown to control both the macroscopic behavior and the microscopic dynamics. Here, we test the generality of the findings of Ref. [16] by studying gels with different particle concentration and interparticle attraction strength. We focus on the sedimentation kinetics and on the asymptotic concentration profiles as the gels attain mechanical equilibrium, showing that the concentration profiles have a universal shape. Using the poroelastic model [14, 15], we show that this remarkable scaling behavior stems from a particularly simple relation between elastic stress and local volume fraction. The rest of the paper is organized as follows: in Sec. 2 we describe the system and the optical methods used to investigate it. The main features of the poroelastic model are recalled in Sec. 3, while Secs. 4.1 and 4.2 report our findings on the asymptotic concentration profiles and the sedimentation kinetics, respectively, before the concluding remarks of Sec. 5.

## 2. Materials and methods

### 2.1. Sample preparation

The colloidal particles are spheres of a polytetrafluoroethylene copolymer (MFA). They have a crystalline core, leading to peculiar optical properties that allow one to measure accurately the local volume fraction, as discussed below. The data presented here are obtained using two different batches, B1 and B2, for which the particle radii are slightly different:  $R_1 = 82 \pm 3$  nm and  $R_2 = 92 \pm 3$  nm, for batches B1 and B2 respectively. The high density  $\rho = 2.14$  g/cm<sup>3</sup> of MFA, combined with its lack of swelling, allows for a precise determination of the initial particle volume fraction  $\varphi_0$  by density measurements. The particles are suspended in an aqueous solution of 0.1M NaCl, to screen electrostatic repulsive interactions, and different amounts of urea were added to suppress coherent polarized scattering by matching the solvent and particle refractive indices. A nonionic surfactant, Triton X100, is added to induce attractive depletion interactions [17], whose range  $r \approx 3$  nm is of the order of the size of the micelles formed

## Sedimentation of $c$

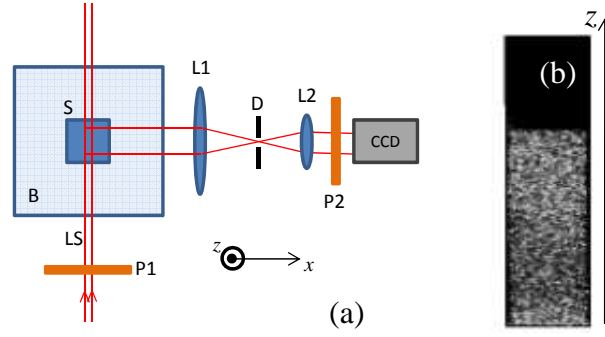


**Figure 1.** (a): schematic top view of the light scattering apparatus. See the text for more details. (b): Typical image of the sample. The gel is the bright, speckled column, the black part is the supernatant.

by the surfactant. In the following we denote by  $\phi_{\text{TX}}$  the concentration of surfactant, defined by  $\phi_{\text{TX}} = V_{\text{TX}}/(V_s - V_p)$ , where  $V_{\text{TX}}$ ,  $V_p$  and  $V_s$  are the volume of the surfactant, that of the particles, and the total volume of the suspension, respectively. A detailed description of the phase behavior of this system can be found in [2]. In brief, the system displays a metastable liquid-liquid coexistence gap; when the amount of added depletant is sufficiently large to drive the colloidal suspension within the coexistence region, as in our case, arrested spinodal decomposition leads to the formation of a disordered gel. All samples described here are deeply in the coexistence region, far from the spinodal line. Because the range of the attractive potential is much smaller than the particle size, our system is well described by Baxter’s adhesive hard sphere model [18]. It is convenient to quantify the strength of the attractive interactions via Baxter’s stickiness parameter  $\tau_{\text{B}}$ . Using methods detailed in [2], we estimate  $\tau \approx 0.01$  for the gels of batch B1 and  $\tau_{\text{B}} \approx 0.02$  for the gels of batch B2 at  $\Phi_{\text{TX}} = 0.11$ .

The samples are prepared by mixing a particle suspension and a surfactant solution with appropriate concentrations; the resulting suspension is loaded in cells with square cross section (either  $3 \times 3 \text{ mm}^2$  or  $5 \times 5 \text{ mm}^2$ ) and filled to an initial height  $h_0 = 22.7 \text{ mm}$  ( $h_0 = 32 \text{ mm}$ ) for batch B1 (B2). The samples are shaken at time  $t_w = 0$  and then left undisturbed for measurements during the sedimentation process.

### 2.2. Light scattering measurements

The apparatus used for light scattering measurements on systems prepared from the first batch is shown in Fig. 1 (a). The sample S is immersed in a transparent water bath B to minimize temperature gradients and temperature fluctuations. It is illuminated by a laser sheet LS, of thickness  $\approx 200 \mu\text{m}$ , height sufficient to cover the whole gel column, and in-vacuo wavelength  $\lambda = 648 \text{ nm}$ . The two lenses L1 and L2 form a demagnified image of the sample onto a charge-coupled detector (CCD) camera. Their focal length is 200 mm and 58 mm, respectively. Two crossed polarizers, P1 and P2, are used to illuminate the sample with light polarized in the vertical direction while detecting

only depolarized scattered light, i.e. light linearly polarized in the horizontal direction. Note that this apparatus combines features of both imaging and scattering [19], since an image of the sample is formed, but using only light scattered around a well-defined scattering wave vector  $q = 4\pi n\lambda^{-1} \sin(\theta/2) = 18.5 \mu\text{m}^{-1}$ , with  $n = 1.356$  the refractive index of the solvent and  $\theta = 90$  deg the scattering angle. A typical image recorded by the CCD is shown in Fig. 1 (b). The gel appears as a speckled, bright column, while the supernatant is black since scattering by the solvent is negligible. Each speckle results from the interference of the light scattered by a small volume in the sample, of depth equal to the laser sheet thickness and lateral size  $\approx 50 \mu\text{m}$ . The speckle size is controlled to about 2 CCD pixels by adjusting the range of  $\theta$  accepted by the detection optics, using the diaphragm D placed in the common focal plane of L1 and L2.

By analyzing a time series of CCD images, we measure four different quantities. The gel total height  $h(t)$  is simply obtained from the height of the bright column. The concentration profiles  $\varphi(z, t)$  are obtained by averaging the intensity  $I$  over regions of interest (ROIs) of height  $\approx 100 \mu\text{m}$  and width equal to the cell width. We emphasize that in general the (polarized) scattered intensity is proportional to both  $\varphi$  and the particle structure factor  $S(q)$ , thus making impossible a determination of the volume fraction based on  $I$  without a detailed knowledge of the sample structure. By contrast, our particles possess a crystalline core and thus partially depolarize the scattered light. As discussed, e.g., in Ref. [20], the depolarized scattered light can be shown to be simply proportional to  $\varphi$ , regardless of the structure. We use an image taken immediately after homogenizing the sample to determine the proportionality constant between  $I$  and  $\varphi$  and to correct for any non-uniformity in the incident beam intensity profile. As the gel sediments, the speckle pattern is shifted downwards: using cross-correlation methods similar to those used in particle imaging velocimetry [21], we are able to measure the full sedimentation velocity profiles,  $v(z, t)$ , with a vertical resolution of about 0.5 mm. Finally, we measure the microscopic dynamics as detailed in Ref. [16], probing in particular particle motion in the horizontal plane, on a length scale of the order of  $q^{-1} \approx R/1.5$ . As a final remark, we emphasize that our measurements of  $\varphi$ , of the microscopic dynamics and, to some extent, of  $v$  all rely on the assumption that the CCD images are formed only by singly scattered photons. Fortunately, the relative low average refractive index of the MFA particles ( $n_p \approx 1.356$ ) allow one to carefully match  $n_p$  using water-based solvents, thereby effectively suppressing multiple scattering.

For systems prepared from the second batch, we use a simplified version of the apparatus shown in Fig. 1, optimized for measuring only  $h(t)$  and  $\varphi(z, t)$  [2]. It consists of a custom-made light scattering setup, operating at a fixed scattering angle  $\theta = 90^\circ$ . Selection of the incident and detected polarization of the scattered intensity is made by means of two Glan-Thomson polarizers with an extinction ratio better than  $1 \times 10^{-6}$ . The cell is mounted on a DC- motorized micrometric translator allowing cell positioning with a resolution of  $0.1 \mu\text{m}$  and an absolute accuracy of about  $3 \mu\text{m}$ . A He-Ne laser beam is mildly focused in the cell to a spot size  $w = 46 \mu\text{m}$ , corresponding to a depth of focus (Rayleigh range) of about 10 mm, fixing the maximum useful optical path in the

cell. The whole setup is enclosed into a removable hood allowing to control temperature to better than  $0.5^\circ C$ .

### 2.3. Visualization of stresses

Valuable information on the distribution of the gravity-induced stress in the sample can be obtained by polarimetry. The sample is illuminated by a collimated beam of white light, issued from a LED source. A demagnified image of the gel is formed onto a CMOS camera, working in transmission. Two crossed polarizers are placed before and after the sample. Under these conditions, for a stress-free sample essentially no light is detected by the camera, because the birefringence induced by the particles is extremely weak. Because stress induces birefringence in the particles [22], regions of the gel where gravity-induced stress accumulates depolarize the incident light and appear as bright in the image (see Fig. 3 below for an example). More precisely [23], when the transmission axes of the polarizers are oriented at  $\pm 45$  deg with respect to the vertical direction, stresses along the horizontal and vertical direction are visualized. Conversely, by turning the polarizers so that their axes are vertical and horizontal, stresses oriented at  $\pm 45$  deg with respect to the vertical direction can be imaged.

## 3. The poroelastic model

We shortly recall here the main features of the poroelastic model, a popular model introduced by Biot [14] and widely used in the literature (see e.g. [15]) to describe the deformation of a gel under its own weight. The system is treated as a continuum medium that responds elastically to a compressive deformation. The effect of the solvent back flow through the gel is accounted for by introducing a viscous friction term. For the sake of completeness, we introduce also a solid friction term, due to the adhesion of the gel to the container walls, which is usually not discussed in the literature.

Typically, the gel sedimentation occurs at a very low Reynolds number and the rate of change of  $v$  is small; thus, inertia terms can be neglected. Using the reference frame shown in Fig. 1 with  $z = 0$  the cell bottom, Newton's law for a gel slice of thickness  $dz$  yields

$$\frac{\partial p}{\partial z} = -\Delta\rho\varphi g - \frac{\partial\sigma}{\partial z} + \frac{\sigma}{L}. \quad (1)$$

Here,  $p$  is pressure,  $\Delta\rho$  the buoyant density,  $g$  the acceleration of gravity,  $\sigma$  the elastic stress, and  $L$  a characteristic length. The term on the l.h.s. originates from the viscous drag, while the terms on the r.h.s. account for the buoyant weight, the elastic stress and the wall friction, respectively. In particular,  $L$  represents Jansen's screening length [24, 25], such that the gravitational stress in a given horizontal plane  $\Sigma$  exerted by a gel slice located  $\Delta z$  above  $\Sigma$  is divided by a factor  $\exp(\Delta z L^{-1})$ . This screening is due to the redirection of part of the gel weight towards the walls. For  $L$  to be finite, the gel must "push" against the walls as it is compressed; in other words, the gel must have

a positive Poisson's ratio  $\nu$ , such that  $L = l(1 - \nu)(\mu\nu)^{-1}$  is finite [24, 25], where  $l$  is side of the square cell section and  $\mu$  is Coulomb's solid friction coefficient. We will show in Sec. 4.1 that for our gels  $\nu \approx 0$  and hence  $L \rightarrow \infty$ . Thus, in the following we shall neglect the wall friction term in Eq. (1).

The conservation of colloidal particles is expressed by the continuity equation:

$$\frac{\partial \varphi}{\partial t} + \frac{\partial}{\partial z}(v\varphi) = 0. \quad (2)$$

The particle velocity  $v$  is related to the viscous stress gradient by Darcy's law [26] via

$$q = -\frac{\kappa(\varphi)}{\eta} \frac{\partial p}{\partial z}, \quad (3)$$

where  $\kappa$  is the volume fraction dependent permeability,  $\eta$  the solvent's viscosity,  $q = (1 - \varphi)(v_s - v)$  the fluid flux in a reference frame co-moving with the gel, and  $v_s$  the solvent velocity in the laboratory frame. Since the volume of the suspension (solvent plus particles) is conserved,  $(1 - \varphi)v_s = -\varphi v$ , which inserted in Eq. (3) yields

$$v = \frac{\kappa(\varphi)}{\eta} \frac{\partial p}{\partial z}. \quad (4)$$

By inserting Eq. (4) in the continuity equation, Eq. (2), and replacing  $\partial p/\partial z$  by the r.h.s. of Eq. (1) with no solid friction term, one finds

$$\frac{\partial \varphi}{\partial t} = \frac{\partial}{\partial z} \left[ \frac{\varphi \kappa(\varphi)}{\eta} \left( \Delta \rho \varphi g + \frac{\partial \sigma}{\partial z} \right) \right]. \quad (5)$$

The final equation describing the temporal evolution of the concentration profiles in the poroelastic model is then

$$\frac{\partial \varphi}{\partial t} = \frac{\partial}{\partial z} \left[ \frac{\varphi \kappa(\varphi)}{\eta} \left( \Delta \rho \varphi g + \frac{K(\varphi)}{\varphi} \frac{\partial \varphi}{\partial z} \right) \right], \quad (6)$$

where we have used the definition of the uniaxial compressional modulus  $K$

$$K(\varphi) = \varphi \frac{\partial \sigma}{\partial \varphi}. \quad (7)$$

In order to solve Eq. (6), the two material functions  $\kappa(\varphi)$  and  $K(\varphi)$  must be specified. Insight on  $K(\varphi)$  may be gained by examining the gel behavior for  $t \rightarrow \infty$ , when the gels approaches mechanical equilibrium. In this limit,  $v$  vanishes and so does the viscous friction. If wall friction is negligible, at any height  $z$  the buoyant weight per unit area of the gel column above  $z$  is balanced by the elastic response of the gel portion below  $z$ :

$$\int_z^{h_\infty} \Delta \rho g \varphi dz = \sigma(z), \quad (8)$$

implying that  $\varphi$  must satisfy

$$\Delta \rho g \varphi = -\frac{\partial \sigma}{\partial z} = -\frac{\partial \sigma}{\partial \varphi} \frac{\partial \varphi}{\partial z}. \quad (9)$$

Experimentally, Eq. (8) can be used to obtain  $\sigma(z)$ , provided that  $\varphi(z)$  can be measured. Once both  $\sigma(z)$  and  $\varphi(z)$  are known, the volume fraction dependence of the elastic stress

is simply obtained by plotting directly  $\sigma$  vs  $\varphi$ . As we will show in Sec. 4.1, for our gels  $\sigma(\varphi)$  is well modeled by a power law:

$$\sigma(\varphi) = A\varphi^\alpha. \quad (10)$$

Assuming this functional form, Eq. (9) can be easily solved:

$$\varphi(z) = \left[ \frac{\Delta\rho g}{A} \frac{\alpha - 1}{\alpha} (z_{\max} - z) \right]^{\frac{1}{\alpha-1}}, \quad (11)$$

where the integration constant  $z_{\max}$  is determined by imposing particle conservation, finding

$$z_{\max}^{\frac{\alpha}{\alpha-1}} - (z_{\max} - h_\infty)^{\frac{\alpha}{\alpha-1}} = h_0 \varphi_0 \left( \frac{\alpha}{\alpha - 1} \right)^{\frac{\alpha}{\alpha-1}} \left( \frac{A}{\Delta\rho g} \right)^{\frac{1}{\alpha-1}}. \quad (12)$$

The determination of the permeability  $\kappa(\varphi)$  is less straightforward. In practice, we test several functional forms proposed for  $\kappa(\varphi)$  and check whether they are able to reproduce the temporal evolution of  $h(t)$ , the total gel height, as we shall discuss it in Sec. 4.2.

(13)

## 4. Results and discussion

### 4.1. Equilibrium concentration profiles

In this section, we focus on the particle volume fraction and interaction strength dependence of the concentration profiles in the long time limit, when no sedimentation is experimentally detectable and the gel is very close to mechanical equilibrium.

For gels of batch B1 and B2, concentration profiles were measured at least 240 and 500 hours after initializing the sample, respectively. We first focus on gels of batch B2. Figure 2a) shows  $\varphi_\infty(z) = \varphi(z, t \rightarrow \infty)$  for three gels, prepared at various particle concentrations  $\varphi_0$  but keeping the same particle interactions ( $\phi_{\text{TX}} = 0.12$ ). The main plot shows that the shape of the concentration profiles does not depend on  $\varphi_0$ : the profiles can be collapsed onto a master curve simply by shifting them along the  $z$  axis so as to make the top part coincide. Thus, the final height of a gel with a given  $\varphi_0$  may be simply predicted using the master curve of Fig. 2 a) and imposing mass conservation. Note that this surprising scaling implies that gels prepared at different  $\varphi_0$  compress in the same way and thus must have the same strength, a counterintuitive result. In fact, we anticipate that these gels are formed by the debris of a percolating network, which is too weak to sustain itself and collapses almost immediately. These debris must have similar structure regardless of  $\varphi_0$ , so that the network resulting from their accumulation at the bottom of the cell has essentially the same mechanical properties.

Interestingly, we observe that the concentration profiles are not very smooth. Measurements of  $\varphi_\infty(z)$  for the same gels but using the ‘‘beam deflection’’ method described in Ref. [27] exhibit a smoother behavior, probably because in the beam

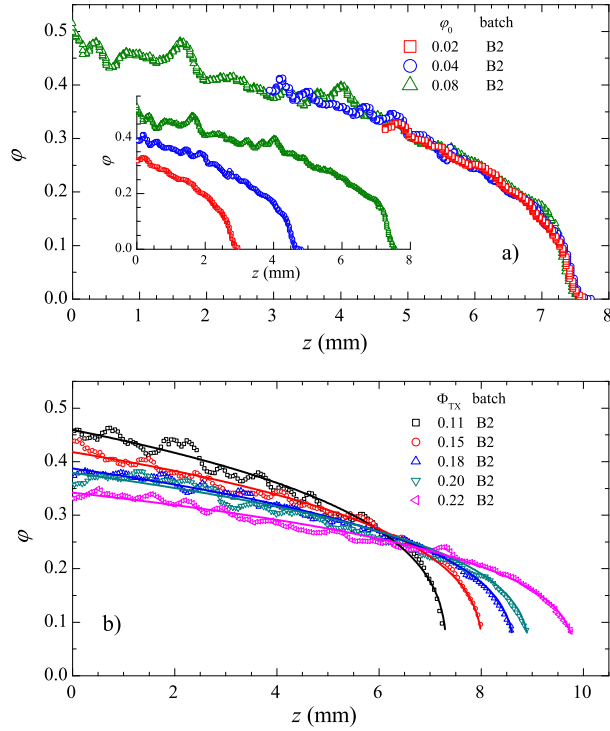


**Figure 2.** Inset of a): asymptotic concentration profiles for gels with fixed  $\phi_{TX} = 0.12$  and various particle concentrations, as indicated in the labels. Main plot of a): same data rescaled onto a master curve as described in the text. b): asymptotic concentration profiles for gels with fixed  $\phi_0 = 0.08$  and various surfactant concentrations, as indicated by the labels. Lines: fits of Eq. (11) to the data.

deflection method the concentration profile is smoothed over a length comparable to the cell optical path (5 mm). The noise in  $\phi$  as measured here may be due also to an extra-contribution to the intensity of the depolarized scattered light stemming from stress-induced birefringence, which we will show below to be spatially non-uniform. In spite of these differences, we emphasize that there is an overall good agreement between  $\phi$  measured by the beam deflection and the depolarized scattered intensity methods [27].

The concentration profiles of gels prepared at a fixed particle concentration  $\phi_0 = 8\%$  and variable interaction strength are shown in Fig. 2 b). As  $\phi_{TX}$  increases, interparticle attractive forces grow and the gel becomes stronger, leading to a smaller compaction under the action of gravity. The change in gel strength is reflected by the fact that the shape of the asymptotic profiles is modified. Indeed, in this case the simple scaling shown in Fig. 2 a) is no more possible.

As discussed in Sec. 3, the asymptotic concentration profile is dictated by the  $\phi$  dependence of the elastic stress  $\sigma$ , which may be obtained directly from the experimental  $\phi_\infty(z)$ , provided that wall friction is negligible. To investigate whether this assumption holds for our gels, we image the distribution of stresses in the gel by polarimetry. The inset of Fig. 3 shows the gel column observed under crossed polarizers, where highly stressed regions are brighter. In the left image, stresses along the vertical and horizontal



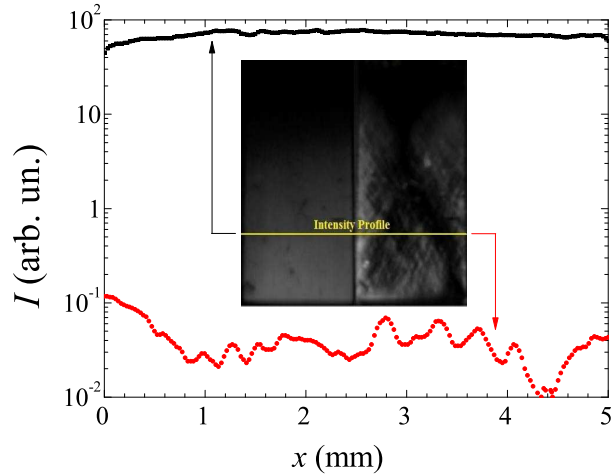


**Figure 3.** Inset: visualization of gravity-induced stress in a gel of batch B2 observed between crossed polarizers ( $\varphi = 0.08, \Phi_{\text{TX}} = 0.12$ ). The height of the image corresponds to the gel height, the width of the cell is 5 mm. In the image on the left (resp., on the right) the polarizers are oriented so as to visualize stress along the vertical and horizontal directions (resp., along directions at  $\pm 45$  deg with respect to vertical). The right image was obtained using an exposure time 1000 times larger than that for the left image. Main plot: intensity level along the horizontal line shown in the images. The intensity levels have been corrected for the difference in exposure time.

direction are *a priori* imaged, although one of course expects vertical stress to dominate. The brightness increases towards the bottom of the cell, a first indication that most of the gravitational stress is transmitted downward, rather than being redirected to the walls. In the right image, the crossed polarizers have been rotated, in order to visualize stress oriented at  $\pm 45$  deg with respect to the vertical direction, which would be non-negligible if wall friction was significant. Although some bright patches do appear, we emphasize that the right image was taken with an exposure time 1000 times larger than for the left one. The intensity profiles along an horizontal line, corrected for the exposure time, clearly show that the vertical component of the stress dominates over that at  $\pm 45$  deg, implying that wall friction can be neglected for our gels. Interestingly, this is at variance with observations for other kinds of colloidal gels [10] and may be due to the fact that here the percolating network initially formed is then broken, in contrast to the gels of Ref. [10].

From the asymptotic concentration profiles shown in Fig. 2 b), we calculate  $\sigma(\varphi)$  as described in Sec. 3 (see Eq. (8)) and plot the result in the inset of Fig. 4 a). The main graph shows that data for all  $\Phi_{\text{TX}}$  can be collapsed onto a single line in a log-log plot, thus indicating that the stress grows with  $\varphi$  as a power law:  $\sigma = A\varphi^\alpha$ . The exponent is essentially the same for all curves, as shown by the good collapse in Fig. 4. By contrast, the prefactor  $A$  depends on  $\Phi_{\text{TX}}$ : stronger bonds (larger  $\Phi_{\text{TX}}$ ) yield a stiffer gel. One expects  $A$  to scale with the interparticle bond spring constant,  $A \sim U_c/r^2$ , where  $U_c$  is the interparticle potential at contact. If the Triton micelles were non-interacting,  $U_c$

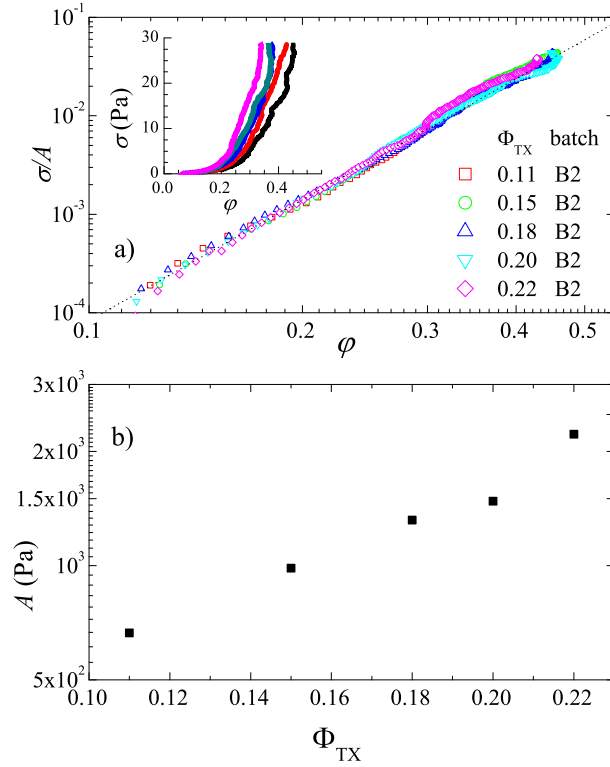


**Figure 4.** Inset of a): elastic stress as a function of  $\varphi$ , for gels with  $\varphi_0 = 0.08$  and  $\Phi_{TX}$  as indicated by the labels. Main plot: scaling of  $\sigma(\varphi)/A$  onto a single power law. The dotted line has slope 4.08. b) Dependence of the scaling factor  $A$  on the amount of depletant.

and thus  $A$  should scale with  $\Phi_{TX}$  [17], whereas Fig. 4 b) rather suggests  $A \sim \exp[\Phi_{TX}]$ . Thus, this behavior hints at deviations with respect to the ideal depletion interaction induced by a diluted gas of micelles.

In principle, both  $A$  and  $\alpha$  may be obtained by fitting  $\sigma(\varphi)$  to a power law. However, we find that a more robust procedure consist in fitting the concentration profiles  $\varphi(z, t \rightarrow \infty)$  to Eq. (11), the expression derived in Sec. 3 for a power law dependence of  $\sigma$  vs  $\varphi$ . The resulting fits are shown as lines in Fig. 2 b). We find that all the concentration profiles for the gels of Fig. 2 b) can be very well fit using the same value  $\alpha = 4.08$ . We furthermore check that the fitting parameter  $z_{\max}$  of Eq. (11) satisfies Eq. (12) to within 2%. It is worth noting that, although  $\sigma$  must eventually diverge as  $\varphi$  approaches the volume fraction of random close packing, no hint of such divergence is observed here, nor in Ref. [16], up to  $\varphi$  values as high as 0.45 (batch B2) or even 0.55 (batch B1).

We check that the law  $\sigma = A\varphi^\alpha$  holds for all gels of both batches, with similar exponents:  $\alpha = 3.6$  (resp., 4.1) for batch B1 (resp., B2). Given the power law dependence of  $\sigma$  vs  $\varphi$ , Eq. (11) suggests that all concentration profiles should collapse on the same straight line when plotting  $\varphi^{\alpha-1}$  vs  $(z - z_{\max})/\ell$ , where  $\ell = A/(\Delta\rho g)$  is a characteristic length scale that compares the gel elasticity to the gravity pull. Figure 5

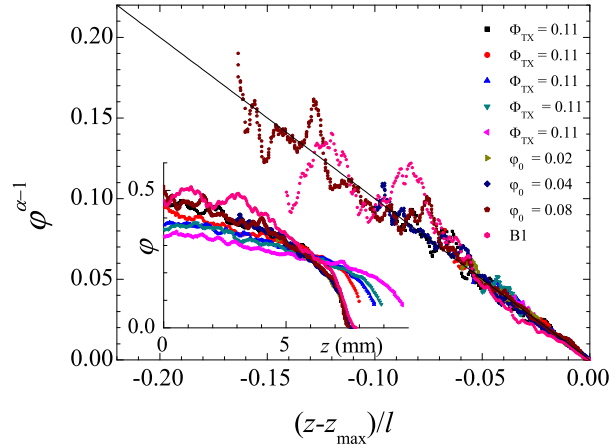


**Figure 5.** Inset: asymptotic concentration profiles for all gels of both batches. Main plot: the same data collapse onto a straight line when using reduced variables, as explained in the text. Data for gels of batch B1 at  $\phi_0 = 0.08$  (resp.,  $\Phi_{\text{TX}} = 0.12$ ) are labeled by  $\Phi_{\text{TX}}$  (resp.,  $\phi_0$ ). For the gel of batch B1,  $\phi_0 = 0.12$ ,  $\Phi_{\text{TX}} = 0.12$ . The line is the poroelastic model.

shows that this is indeed the case for all the gels we have studied.

#### 4.2. Sedimentation kinetics

The temporal evolution of the total height of the gel,  $h$ , exhibits a qualitatively similar behavior for all the gels of batches B1 and B2. Denoting by  $t_w$  the time after filling the sample cell, an initial regime where no sedimentation occurs is observed for  $t_w < t_d$ . The latency time  $t_d$  grows with the strength of interparticle bonds and  $\phi_0$ , as observed in previous works [4, 5, 6, 7, 8]. During this phase, the speckle dynamics is essentially frozen, indicating that a system-spanning arrested network has been formed. For  $t_d \leq t_w < t_c$ ,  $h$  decreases steeply and the speckles fluctuate rapidly, indicating that the network has failed under gravitational stress. Finally, for  $t_w \geq t_c$  the falling debris of the initial network have deposited at the bottom of the cell, forming a denser gel, as indicated by the dramatic slowing down of the speckle dynamics. This denser gel slowly compacts under its own weight: we define  $t = t_w - t_c$  and describe the gel evolution in this third regime using the poroelastic model of Sec. 3. An example of  $h(t_w)$  for a gel of batch B1 is shown in Fig. 6 a). Here, network failure occurs almost immediately,  $t_d \approx 0$ . Note that  $h(t_w)$  is almost identical for gels prepared in cells with square sections equal to  $3 \times 3 \text{ mm}^2$  and  $5 \times 5 \text{ mm}^2$ , thus confirming that wall effects are negligible. Interestingly, during the initial collapse  $h(t_w)$  decreases linearly in time, as observed also for gels of the second batch prepared at various  $\phi_0$ , see Fig. 6 b). This behavior is in striking contrast with that reported very recently by Bartlett *et al.* [8], who find a “compressed exponential” decrease,  $h(t_w - t_d) \sim \exp\{-[(t_w - t_d)/\tau_c]^{1.5}\}$ . This difference might be due to the different range of the attractive potential, which is small in our case ( $r/R \approx 0.037$ ) and much larger in Ref. [8] ( $r/R \approx 0.62$ ). More experiments will be

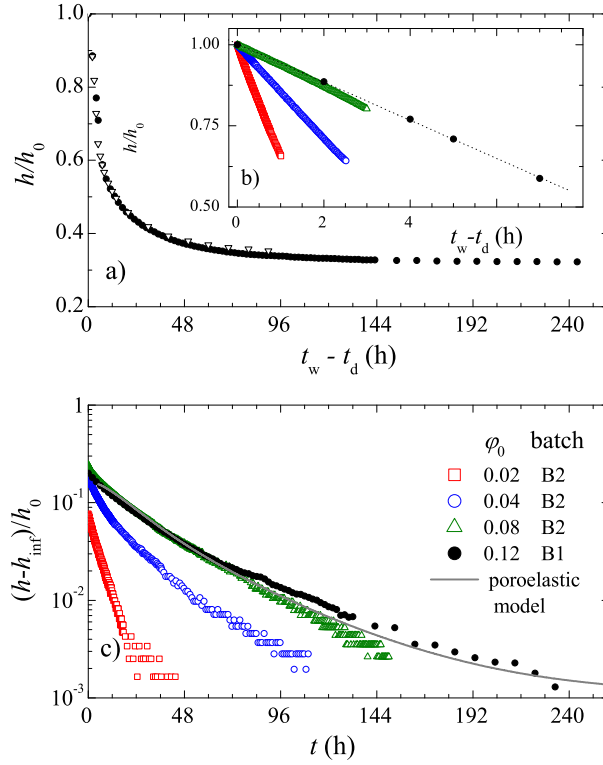


**Figure 6.** a): time evolution of the total height for a gel of batch B1 with  $\varphi = 0.12$ ,  $\phi_{\text{TX}} = 0.12$ . The cell section is  $3 \times 3 \text{ mm}^2$  ( $5 \times 5 \text{ mm}^2$ ) for the solid circles (open triangles),  $h_0 = 22.7 \text{ mm}$ . b): initial decay of  $h$  during the collapse of gels of both batches (same symbols as in c)): in all cases, a linear behavior is observed. c) semilogarithmic plot of the time varying part of  $h$  normalized by  $h_0$ , during the compaction regime. The line is a fit of the poroelastic model to the data for the gel of batch B1.

needed to elucidate this point. Figure 6 c) shows the time-varying part of  $h$  during the compaction stage, for various  $\varphi_0$ . The decay of  $h$  is not a simple exponential, as shown by the curvature of the data in a semilogarithmic plot. Indeed, we find that the data can be reasonably well fit by a stretched exponential function,  $h(t) - h_\infty \sim \exp[-(\Gamma t)^\beta]$ , with  $\beta = 0.68 - 0.87$ , depending on sample composition (fit not shown). Although the stretched exponential fit works well, it has no obvious theoretical interpretation, besides the generic remark that the system exhibits a distribution of relaxation times. A better justified fit is provided by the prediction of the poroelastic model, Eq. (6), which we solve numerically for the gel of batch B1 [16] and show as a continuous line in Figure 6 c). As discussed in Sec. 3, the permeability  $\kappa(\varphi)$  must be provided in order to solve Eq. (6). By testing various functional forms, including those proposed in the past for gels with a fractal structure [12], we find that only a critical-like law similar to that used for suspensions of hard spheres is able to reproduce our results:  $\kappa(\varphi) = \kappa_0 \varphi^{-1} (1 - \varphi)^m$ , with  $m = 7$ . The remarkable success of the poroelastic model is demonstrated by the fact that, having determined  $K(\varphi)$  and  $\kappa(\varphi)$  from fits of  $\varphi(z, t \rightarrow \infty)$  and  $h(t)$ , respectively,

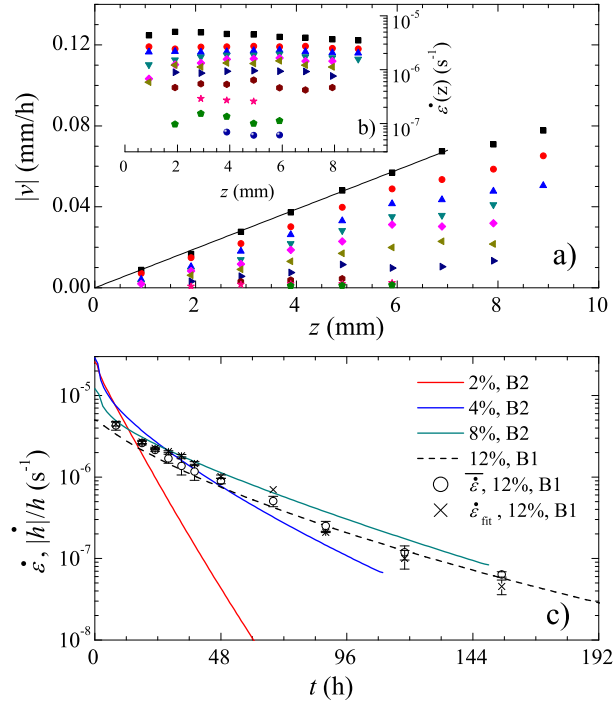


**Figure 7.** a) sedimentation velocity  $vs$  height at various times, ranging from  $t_w = 30\text{h}$  to  $t_w = 167\text{h}$  from top to bottom, for a B1 gel with  $\varphi = 0.12$ ,  $\Phi_{\text{TX}} = 0.12$ . The line is a linear fit to  $v(z, t_w = 30\text{h})$  up to  $z = 7$  mm. b): strain measured over a height  $z$ ,  $\dot{\epsilon} = |v|/z$ , for the same data as in a). c): global strain  $|\dot{h}|/h$  (dotted line),  $z$ -averaged strain  $\bar{\epsilon}$  (open circles) and  $\epsilon_{\text{fit}}$  as defined in the text, for the same gel as in a) and b). The solid lines are  $|\dot{h}|/h$  for the three gels of batch B2 shown in Fig. 6, for which  $\Phi_{\text{TX}}$  increases from left to right.

the solution to Eq. (6) reproduces very well the full time evolution of the concentration and velocity profiles, as reported in Ref. [16].

One of the most surprising findings of Ref. [16] is the linear variation of the sedimentation velocity  $v$  with height  $z$  in the gel column. Figure 7 a) shows that indeed  $|v| \sim z$ , at least for the lower part of the gel column. Close to the top, deviations from this linear behavior appear, in that  $v$  appears to grow more slowly with  $z$ . These deviations are more pronounced for longer times. We define a compressive strain rate,  $\dot{\epsilon}_{\text{fit}}$ , as the slope of a linear fit to  $v(z)$  in the regime where a linear behavior is observed, e.g. up to  $z = 7$  mm for data at  $t_w = 30\text{h}$  in Fig. 7 a). We also define the strain rate measured at height  $z$  as  $\dot{\epsilon}(z) = v/z$  and plot its height dependence in Fig. 7 b). This quantity is almost independent of  $z$ , with the exception of the very bottom and top parts of the gel column, thus confirming that the temporal evolution of the full velocity profiles is essentially captured by the evolution of a single parameter,  $\dot{\epsilon}$ . Additionally, we have shown in Ref. [16] that  $\dot{\epsilon}$  governs also the microscopic dynamics, since structural rearrangements occur on a time scale  $\tau_\alpha$  such that  $\tau_\alpha \dot{\epsilon} = \epsilon_y$ , where  $\epsilon_y \approx 0.02$  is the typical yield strain beyond which irreversible rearrangements occur. In view of the key role played by  $\dot{\epsilon}$ , it is interesting to test whether a macroscopic

measurement of the global strain rate,  $|\dot{h}|/h$ , reflects accurately the microscopic strain rate. In Fig. 7 c) we compare for a gel of batch B1  $|\dot{h}|/h$  (dotted line) to  $\dot{\epsilon}_{\text{fit}}$  (crosses) and  $\bar{\epsilon}$ , the average of  $\dot{\epsilon}(z)$  over the gel height (open circles). In order to reduce the impact of the measurement noise on the numerical derivative of  $h(t)$ , we differentiate the stretched exponential fit of  $h(t)$  discussed in reference to Figure 6 c), rather than the data themselves. Figure 7 c) shows that a reasonably good agreement is found between these three ways of quantifying the compressive strain rate, thus demonstrating that deviations from the linear behavior of  $v(z)$  are limited. To check the generality of our findings we simulate the time evolution of gels with different value of  $K(\varphi)$  and  $\kappa(\varphi)$ . In all cases we have studied,  $|v| \sim z$  in the lower part of the gel column while, close to the top,  $v$  grows slower with  $z$ . Besides  $\dot{\epsilon}_{\text{fit}}$ ,  $\dot{\epsilon}(z)$  and  $|\dot{h}|/h$  are strongly correlated. In particular, we found that  $|\dot{h}|/h < \dot{\epsilon}(z) = v/z < \dot{\epsilon}_{\text{fit}} \approx A|\dot{h}|/h$  with  $1 < A < 1.35$  depending on the functional form of  $K(\varphi)$  and  $\kappa(\varphi)$ , so that  $\dot{\epsilon}$  may be directly estimated from  $|\dot{h}|/h$ . This observation can be particularly useful when dealing with turbid samples, where the velocity profiles can not be measured directly.

Figure 7 c) shows also the macroscopic strain rate for the same three gels of batch B2 as in Figs. 2 a) and 6. In spite of the variation of  $\varphi_0$ , the strain rate at the beginning of the compaction stage is of the same order of magnitude for all samples. This is probably due to the fact that the structure of the gel is similar, as discussed in relation to the scaling of the concentration profiles shown in Fig. 2 a). By contrast, the temporal evolution of the strain rate is significantly different,  $|\dot{h}|/h$  decaying faster for the gels at lower initial  $\varphi$ . This is at odd with the scaling behavior of the concentration profiles reported in Fig. 2a, where it was shown that the top part of the gels at fixed  $\Phi_{\text{TX}}$  have the same concentration profile. This can be qualitatively understood by recalling that, although the top of the profiles for samples prepared at different  $\varphi_0$  are similar (see Fig.4.1), gels prepared at higher initial concentration reach a higher volume fraction at the cell bottom. Therefore, they display in this region a lower permeability and a higher stiffness, which slows down the compaction process.

## 5. Conclusions

We have studied the sedimentation kinetics and the concentration profiles of depletion-induced colloidal gels, varying both the particle volume fraction and the strength of the interparticle interactions. By using optical methods that combine light scattering and imaging, we have been able to gain detailed information on the evolution of the concentration profiles and the dynamics of the gels. Coupled to stress visualization experiments that rule out any significant role of solid friction on the cell walls, this has allowed us to measure quantitatively the volume fraction dependence of the elastic response of the gels and to test thoroughly the poroelastic model. In discussing the  $\varphi_0$  and  $\Phi_{\text{TX}}$  dependence of the parameters issued from the poroelastic model, it is essential to keep in mind that the model can only be applied to the last regime of the sedimentation process, i.e. the compaction of a denser gel formed by the falling

debris of the initial network that fails under gravity. This allows one to rationalize some apparently paradoxical results, such as the scaling of the asymptotic concentration profiles obtained at fixed  $\Phi_{TX}$  and variable  $\varphi_0$ .

Our work and that of other groups using confocal microscopy [6, 8] show that detailed microscopic information on the structure and the dynamics of the gels can be very valuable in order to better understand the behavior of colloidal gels under gravitational stress. More work along these lines will be required to fully understand the microscopic origin of the diversity of behaviors observed for different systems.

## Acknowledgments

We thank L. Berthier for many useful discussions and Solvay-Solexis for having provided us the Hyflon<sup>TM</sup> MFA particle batch. Financial support from Région Languedoc Roussillon, CNES, ANR “Dynhet”, the Italian Ministry of Education and Research (MIUR) (PRIN 2008) and ASI is gratefully acknowledged.

## References

- [1] Zaccarelli E. *J. Phys.:Condens. Matter*, 19(32):323101, 2007.
- [2] Buzzaccaro S, Rusconi R, and Piazza R. *Phys. Rev. Lett.*, 99:098301, 2007.
- [3] Lu PJ, Zaccarelli E, Ciulla F, Schofield A, Sciortino F, and Weitz DA. *Nature*, 453(7194):499–503, 2008.
- [4] Starrs L, Poon WCK, Hibberd DJ, and Robins MM. *J. Phys.:Condens. Matter*, 14(10):2485–2505, 2002.
- [5] Kilfoil ML, Pashkovski EE, Masters JA, and Weitz DA. *Philos. Trans. R. Soc. A-Math. Phys. Eng. Sci.*, 361(1805):753–766, 2003.
- [6] Huh JY, Lynch ML, and Furst EM. *Phys. Rev. E*, 76, 2007.
- [7] Buscall R, Choudhury TH, Faers MA, Goodwin JW, Luckham PA, and Partridge SJ. *Soft Matter*, 5(7):1345–1349, 2009.
- [8] Bartlett P, Teece LJ, and Faers MA. *arxiv*, page 1109.4893, 2011.
- [9] Allain C, Cloitre M, and Wafra M. *Phys. Rev. Lett.*, 74(8):1478–1481, 1995.
- [10] Condre JM, Ligoure C, and Cipelletti L. *J Stat Mech - Theory and Experiments*, page P02010, 2007.
- [11] Manley S, Skotheim JM, Mahadevan L, and Weitz DA. *Phys. Rev. Lett.*, 94(21):218302, 2005.
- [12] Kim C, Liu Y, Kuhnle A, Hess S, Viereck S, Danner T, Mahadevan L, and Weitz DA. *Phys. Rev. Lett.*, 99(2):028303, 2007.
- [13] Derec C, Senis D, Talini L, and Allain C. *Phys. Rev. E*, 67(6):062401, 2003.
- [14] Biot MA. *J. Appl. Phys.*, 12:155–164, 1941.
- [15] Buscall R and White LR. *J. Chem. Soc., Faraday Trans.*, 83:873–891, 1987.
- [16] Brambilla G, Buzzaccaro S, Piazza R, Berthier L, and Cipelletti L. *Phys. Rev. Lett.*, 106:118302, 2011.
- [17] Asakura S and Oosawa F. *J. Chem. Phys.*, 22:1255–1256, 1954.
- [18] Baxter RJ. *J. Chem. Phys.*, 49:2770–2774, 1968.
- [19] Duri A, Sessoms DA, Trappe V, and Cipelletti L. *Phys. Rev. Lett.*, 102(8):085702–4, 2009.
- [20] Buzzaccaro S, Piazza R, Colombo J, and Parola A. *J. Chem. Phys.*, 132(12):124902, 2010.
- [21] Tokumaru PT and Dimotakis PE. *Exp. Fluids*, 19:1–15, 1995.
- [22] Mueller H. *J. Appl. Phys.*, 6:179–184, 1935.
- [23] Coker EG and Filon LNG. *Treatise on Photoelasticity*. Cambridge Press, 1930.

- [24] Bouteux T, Raphaël E, and de Gennes PG. *Phys. Rev. E*, 55(5):5759–5773, 1997.
- [25] Ovarlez G, Fond C, and Clément E. *Phys. Rev. E*, 67(6):060302, 2003.
- [26] Darcy H. *Les Fontaines Publiques de la Ville de Dijon*. Dalmont, Paris, 1856.
- [27] Piazza R, Buzzaccaro S, and Secchi E. *J. Phys.: Condens. Matter*, this issue, 2011.